Sensors & Transducers, Vol. 207, Issue 12, December 2016, pp. 36-43

www.sensorsportal.com

Sensors & Transducers

Published by IFSA Publishing, S. L., 2016
http://www.sensorsportal.com

Preliminary Studies on Capacitive Proximity Sensing for Touchless Interaction with a Human Finger

*** Leonhard HASLINGER and Bernhard G. ZAGAR**
Johannes Kepler University Linz, Institute for Measurement Technology, Altenberger Straße 69, 4040 Linz, Austria
Tel.: +43 732 2468 5923, fax: +43 732 2468 5933
* E-mail: leonhard.haslinger@jku.at

Received: 5 November 2016 /Accepted: 5 December 2016 /Published: 30 December 2016

Abstract: This contribution deals with preliminary studies for touchless interaction based on capacitive sensor technologies. An existing approach in combination with additional capacitance measurements is used for position estimation. For that, a measurement system is utilized which is able to measure capacitances in a range of a few fF to several pF. The main focus is the 3D position estimation of a human finger through measuring the spatial capacitance distributions caused by its movements. A grounded metallic test object is used as an abstract model of a finger. The capacitance modeling is based on a 2D simplification by considering properties of symmetry. This new model, combined with complex data processing algorithms, ensures precise finger gesture recognition in future research.

Keywords: Modeling, 3D position estimation, Capacitive proximity sensors, Touchless interaction, Electric field.

1. Introduction

Numerous scientific publications in the context of touchless interaction, which are based on capacitive sensor technologies, deal with machine learning methods [1-2]. For an implementation of these algorithms empirical approximations, and a set of training data are often sufficient [3].

In contrast, this contribution uses a novel approach [4] that leads to a deeper physical understanding and model-based accurate algorithms for touchless interaction. Based on the proposed capacitance model 3D position estimation [5] can be implemented. Subsequently, tracking a sequence of positions should enable gesture recognition in future work. Here, a moderate spatial resolution of the measurement system is acceptable if the time resolution is sufficient to recognize smooth motions. The typically encountered small capacitance values and the rapid capacitance changes caused by finger movements render the system sensitive to interferences. Concerning this matter the measurement and online evaluation of the data is challenging and already partly discussed in [6]. Furthermore, a variety of finger forms as well as numerous possible environmental conditions and disturbances are not considered. The main target regarding touchless interaction is to recognize the user's intention. In the case of incorrect interpretation an active feedback can inform the user how his behavior must be changed for a subsequent clear recognition.

Fig. 1 shows a schematic of the measurement set-up consisting of a sensing electrode with an area $a_s \times a_s$, a shielding electrode and a human finger. The surrounding volume is assumed as free space modeled with the permittivity ε_0. For measurements, a grounded brass cuboid with an area $a_t \times a_t$ and a height h_t above the sensor plane is used as an abstract model

for an interacting finger, where the coordinates x_t, y_t and z_t describe the center position of its tip (denoted by an x in Fig. 1). In general, the human body capacitance to ground is about 150 pF [7]. This value is significantly larger than the maximal expected capacitance value[1] in the gesture sensing application. Therefore, a ground connected brass cuboid is a favorable simplification for a human finger.

The excitation signal is applied to the sensing electrode, which is used to measure the capacitance C_{3D} to ground. With a guard amplifier the shielding electrode is served to the same potential as the sensing electrode. Thereby, the effect or influence of parasitic capacitances is kept in check.

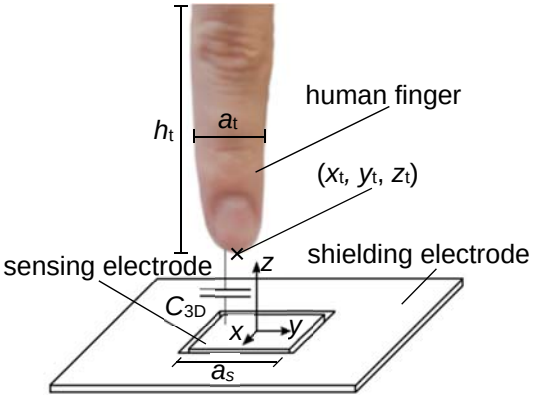

Fig. 1. Schematic of the measurement set-up.

Table 1 shows the values of the dimensions in Fig. 1 which are used for all the presented measurement data.

Table 1. Parameters for the measurement.

Description	Parameter	Value
Width of electrode	a_s	15 mm
Width of cuboid	a_t	15 mm
Height of cuboid	h_t	55 mm

Due to symmetry properties, the 3D problem in Fig. 1 is presented as planar 2D problem in section 'Capacitance Modeling'. This configuration is divided in further parts for a mathematical description of the spatial capacitance distribution. These partial solutions of the 2D problem are combined for a 3D capacitance model. Section 'Capacitance Measurement' contains details concerning the measurement system, and the measured values are compared with the 3D capacitance model. Further, section 'Results' presents 3D position estimation as a basis for touchless interaction of a human finger. Finally, section 'Conclusion' discusses advantages and disadvantages as well as possible improvements for the 3D position estimation. Moreover, an outlook presents open problems for further studies.

[1] The parallel plate capacitor model at 1 mm plate distance yields 2 pF.

2. Capacitance Modeling

Since an analytical calculation of C_{3D} in Fig. 1 is sophisticated, simplifications are useful. These simplifications are based on [8] and were partially discussed in [4].

2.1. 2D Modeling

Fig. 2 illustrates the abstraction of the measurement set-up in Fig. 1 as a planar problem in the *xz*-plane for y = 0. It is necessary to scale quantities in Fig. 2 with the spatial dimension a_y in *y*-direction to be consistent with Fig. 1. In Fig. 2 the corresponding human finger from Fig. 1 is assumed by a grounded metallic cuboid as test object. Furthermore, Fig. 2 splits the total capacitance into the capacitance C_b between the base of the cuboid and ground as well as the capacitances C_{sl} and C_{sr} between the left and right side of the cuboid and ground. The capacitance between the top side of the cuboid and ground is negligible. Therefore, the total capacitance C_{2D} between the sensing electrode and the cuboid follows as

$$C_{2D} = C_b + C_{sl} + C_{sr}\,, \tag{1}$$

where the x_t and z_t dependency of the capacitances is not denoted explicitly.

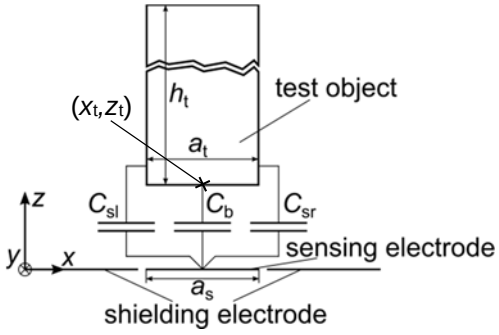

Fig. 2. Schematic of the planar problem.

For modeling C_b, C_{sl} and C_{sr} further simplifications are assumed:

- The spatial extension of the sensing and shielding electrode in *z*-direction are neglected.
- The gap between the sensing and the shielding electrode in the *xy*-plane is modeled as infinitesimally small.
- The shielding electrode extends infinitely in the *xy*-plane.

Modeling of C_b

The modeling of C_b is based on the geometry in Fig. 3. The superposition of two in x-direction differently shifted geometries in Fig. 3 follows in an approximation for C_b. The bottom Electrode 2 (red) and the bottom Shield 2 (blue) are part of the sensing and shielding electrode in Fig. 2. The top Electrode 1 (red) is part of the base area of the test object in Fig. 2. There is no equivalent for the top Shield 1 (blue), because it is used for virtual shielding of the partial capacitances C_{sl} and in the shifted case for the virtual shielding of the partial capacitance C_{sr}. Furthermore, the additional Shield 1 mainly results in a simplification for the mathematical calculation (superposition). At the point $x = x_1$ and $z = z_d$ Shield 1 ends and Electrode 1 begins and at point $x = x_2$ and $z = 0$ Electrode 2 ends and Shield 2 begins. Between the Electrodes 1 and 2 voltage U_{12} is applied. Moreover, the geometry is divided in part I ($x \leq x_1$) and part II ($x > x_1$) for a convenient calculation of the potential distribution.

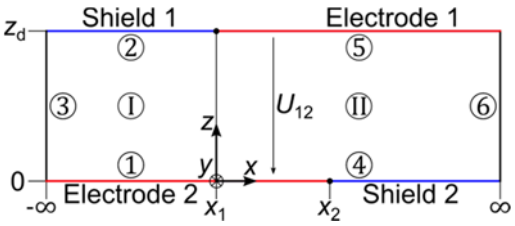

Fig. 3. Geometry definition for the modeling of C_b.

The potential φ within the electrode geometry in Fig. 3 follows as

$$\varphi(x,z) = \begin{cases} \varphi_{\mathrm{I}}(x,z) & \text{for } x \leq x_1 \\ \varphi_{\mathrm{II}}(x,z) & \text{for } x > x_1 \end{cases} \tag{2}$$

with the potential φ_{I} in part I and the potential φ_{II} in part II. The boundaries are divided into parts ① to ⑥ with the potentials given in Table 2.

Tab. 2. Parameters for the measurement.

Boundary	x	z	φ
①	$x \leq x_1$	$z = 0$	0
②	$x \leq x_1$	$z = z_d$	0
③	$x \to -\infty$	$0 < z < z_d$	0
④	$x > x_1$	$z = 0$	0
⑤	$x > x_1$	$z = z_d$	U_{12}
⑥	$x \to \infty$	$0 < z < z_d$	$U_{12}\frac{z}{z_d}$

For the unique solution of the Laplace's equation [9]

$$\Delta\varphi(x,z) = 0 \tag{3}$$

additional constraints at the transition between part I and II are necessary. These are the Dirichlet condition

$$\varphi_{\mathrm{I}}(x_1,z) = \varphi_{\mathrm{II}}(x_1,z) \text{ for } 0 < z < z_d \tag{4}$$

and the Neumann condition

$$\frac{d\varphi_{\mathrm{I}}(x_1,z)}{dx} = \frac{d\varphi_{\mathrm{II}}(x_1,z)}{dx} \text{ for } 0 < z < z_d \tag{5}$$

To obtain a solution of (3) for the boundary conditions listed in Table 2 and the transition conditions (4) and (5) a separation of variables is suggested in [8]. This leads to the partial potentials φ_{I} and φ_{II} represented as

$$\varphi_{\mathrm{I}}(x,z) = \frac{U_{12}}{\pi}\sum_{n=1}^{\infty}\frac{(-1)^{n+1}}{n}e^{\frac{-n\pi|x-x_1|}{z_d}}\sin\left(\frac{n\pi z}{z_d}\right) \tag{6.a}$$

$$\varphi_{\mathrm{II}}(x,z) = U_{12}\frac{z}{z_d} - \varphi_{\mathrm{I}}(x,z) \tag{6.b}$$

Besides, with (6) the surface charge density σ_2 on Electrode 2 in Fig. 3 follows through

$$\sigma_2(x) = -\varepsilon_0\frac{\partial\varphi(x,0)}{\partial z} = -\varepsilon_0\frac{U_{12}}{z_d}\frac{e^{\frac{\pi(x-x_1)}{z_d}}}{1+e^{\frac{\pi(x-x_1)}{z_d}}} \tag{7}$$

The superposition of the electric fields for the configuration in Fig. 3 with

$$x_1 = x_t - \frac{a_t}{2}, x_2 = \frac{a_s}{2} \tag{8}$$

and another configuration with an inverted potential distribution at the boundaries

$$x_1 = x_t + \frac{a_t}{2}, x_2 = -\frac{a_s}{2} \tag{9}$$

results in the field distribution, which is necessary for modeling C_b in Fig. 2. Consequently, the charge density σ_s on the sensing electrode is described by

$$\sigma_s(x) = -\sigma_2(x)|_{x_1=x_t-\frac{a_t}{2}} + \sigma_2(x)|_{x_1=x_t+\frac{a_t}{2}} \tag{10}$$

through superposition. By means of (10) the electric charge Q_s on the sensing electrode follows as

$$Q_s = a_y\int_{-\frac{a_s}{2}}^{\frac{a_s}{2}}\sigma_s(x)\,dx \tag{11}$$

Thereby, C_b can be calculated over the capacitance definition

$$C_b = \frac{Q_s}{U_{12}} \tag{12}$$

to

$$C_b = a_y\frac{\varepsilon_0}{\pi}\ln\left(\frac{\cosh(k_{b1})\cosh(k_{b2})}{\cosh(k_{b3})\cosh(k_{b4})}\right) \tag{13}$$

with x_t and z_t dependence parameter k_{b1}, k_{b2}, k_{b3} and k_{b4}. Through the expressions

$$k_{b1} = \frac{\pi}{4z_t}(2x_t - a_s - a_t), \quad (14.a)$$

$$k_{b2} = \frac{\pi}{4z_t}(2x_t + a_s + a_t), \quad (14.b)$$

$$k_{b3} = \frac{\pi}{4z_t}(2x_t + a_s - a_t), \quad (14.c)$$

$$k_{b4} = \frac{\pi}{4z_t}(2x_t - a_s + a_t) \quad (14.d)$$

these parameters are determined. Assuming the same width $a_t = a_s$ (cf. Tab. 1) for the test object and the sensing electrode, C_b can be simplified to

$$C_b = a_y \frac{\varepsilon_0}{\pi} \ln\left(\frac{1}{2}\cosh\left(\frac{\pi a_s}{z_t}\right) + \frac{1}{2}\right) \quad (15)$$

at $x_t = 0$. For $a_s/z_d \gg 1$ the capacitance C_b results in the well known parallel plate capacitor model

$$C_b \approx \varepsilon_0 \frac{a_y a_s}{z_t} \quad (16)$$

Modeling of C_{sl} and C_{sr}

The conformal map f from [9-10] expressed as

$$t = f(s) = \ln(s) \quad (17)$$

in Fig. 4 is the basis for the approximation of C_{sl} and C_{sr}. This conformal map is a transformation from the s-plane

$$s = x + jz \quad (18)$$

into the t-plane

$$t = \xi + j\varsigma \quad (19)$$

Fig. 4 shows the relation between the radial geometry with the radii r_{o1}, r_{o2}, r_{u1} and r_{u2} as well as the angle α in the s-plane and the problem in the t-plane. The problem in the t-plane is equivalent to the planar problem for the calculation of C_b before (cf. Fig. 2).

For calculating C_{sr} with (17) three geometrical sections of the form

$$\text{section 1: } -\frac{a_s + a_t}{2} > x_t, \quad (20.a)$$

$$\text{section 2: } -\frac{a_s + a_t}{2} \le x_t < \frac{a_s - a_t}{2}, \quad (20.b)$$

$$\text{section 3: } \frac{a_s - a_t}{2} \le x_t \quad (20.c)$$

are distinguished. The sections are referenced via the x-position x_t of the test object.

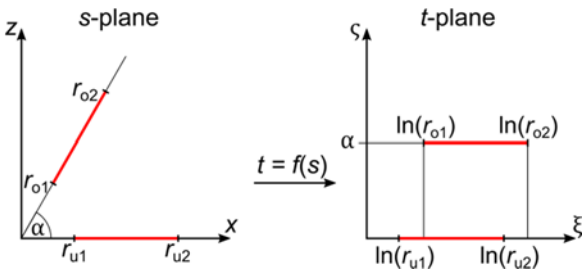

Fig. 4. Conformal map from s-plane into t-plane.

Fig. 5 depicts a schematic of Sections 1 and 2. There is a relative coordinate system with axes x' and z', that moves in x-direction with the test object.

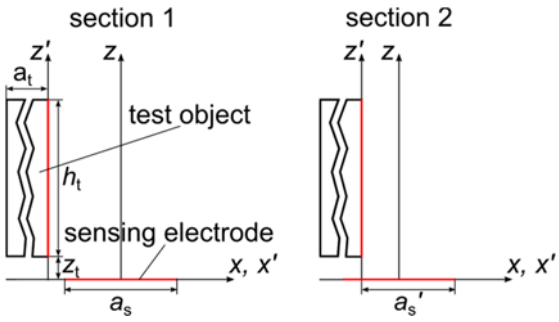

Fig. 5. Schematic of Sections 1 and 2.

Hence, the parameters in Fig. 4 for Section 1 follow as

$$r_{o1} = z_t\,, \qquad r_{o2} = r_{o1} + h_t \quad (21.a)$$

$$r_{u1} = -\frac{a_s + a_t}{2} - x_t\,, \qquad r_{u2} = r_{u1} + a_s \quad (21.b)$$

$$\alpha = \frac{\pi}{2} \quad (21.c)$$

In Section 2 the effective width of the sensing electrode is reduced from a_s to a_s'. The parameters in Fig. 5 are given by

$$r_{u1} = 0\,, \qquad r_{u2} = a_s' \quad (22)$$

whereby (21.a) and (21.c) do not change. Section 3 is not part of Fig. 5 because there is $a_s' = 0$ and the parameters are determined by

$$r_{u1} = 0\,, \qquad r_{u2} = 0\,, \quad (23)$$

thus not contributing any capacitance. Further, with (21), (22) and (23) in the t-plane (cf. Fig. 4) the equivalent problem must be solved for the capacitance calculation for C_b. Analogously to (13) and (14) the capacitance C_{sr} results in

$$C_{\mathrm{sr}} = a_{\mathrm{y}} \frac{\varepsilon_0}{\pi} \ln\left(\frac{\cosh(k_{\mathrm{sr1}})\cosh(k_{\mathrm{sr2}})}{\cosh(k_{\mathrm{sr3}})\cosh(k_{\mathrm{sr4}})}\right) \qquad (24)$$

and with (21), (22) and (23)[2] for the parameters k_{sr1}, k_{sr2}, k_{sr3} and k_{sr4} the expressions

$$k_{\mathrm{sr1}} = \frac{\pi}{2\alpha}(\ln(r_{\mathrm{u2}}) - \ln(r_{\mathrm{o1}})) \qquad (25.a)$$

$$k_{\mathrm{sr2}} = \frac{\pi}{2\alpha}(\ln(r_{\mathrm{u1}}) - \ln(r_{\mathrm{o2}})) \qquad (25.b)$$

$$k_{\mathrm{sr3}} = \frac{\pi}{2\alpha}(\ln(r_{\mathrm{u1}}) - \ln(r_{\mathrm{o1}})) \qquad (25.c)$$

$$k_{\mathrm{sr4}} = \frac{\pi}{2\alpha}(\ln(r_{\mathrm{u2}}) - \ln(r_{\mathrm{o2}})) \qquad (25.d)$$

follow. The reduction of the effective width of the sensing electrode from a_{s} to a_{s}' causes negligible partial capacitances. Moreover, in Section 3 capacitance contributions are completely omitted and therefore $C_{\mathrm{sr}} = 0$. The capacitance calculation for C_{sl} can be done in the same way as for C_{sr} in (24) and (25).

2.2. 3D Modeling

To evaluate the validity of the derived 2D model approximating the 3D reality some further investigations are necessary.

Fig. 6 shows the capacitance contour lines[3] of C_{3D} for $z_{\mathrm{t}} = 2$ mm and $z_{\mathrm{t}} = 5$ mm in the xy-plane.

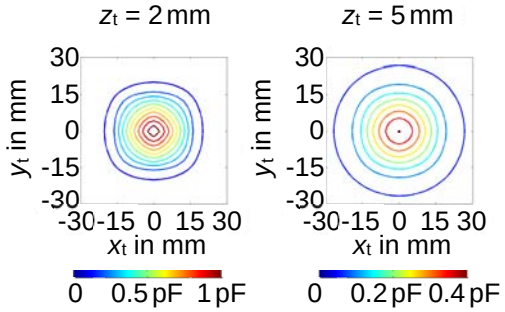

Fig. 6. Contours of C_{3D} for $z_{\mathrm{t}} = 2$ mm and $z_{\mathrm{t}} = 5$ mm.

As a consequence of the rectangular forms of sensing electrode and test object the contours differ from the circular form in the short range (see Fig. 6 for $z_{\mathrm{t}} = 2$ mm). For larger distances the capacitance contours are nearly circular (see Fig. 6 for $z_{\mathrm{t}} = 5$ mm).

Therefore, an approximation for the 3D capacitance model C_{3D} follows as

$$C_{\mathrm{3D}}(x_{\mathrm{t}}, y_{\mathrm{t}}, z_{\mathrm{t}}) = C_{\mathrm{2D}}\left(\sqrt{{x_{\mathrm{t}}}^2 + {y_{\mathrm{t}}}^2}, z_{\mathrm{t}}\right) \qquad (26)$$

In the following this approach is used for small as well as for large distances and the validity is verified by measurements.

3. Capacitance Measurement

Fig. 7 shows the measurement system consisting of a 3-axis translation stage, the test object, the sensing electrode array and the extended OpenCapSense hardware with eight channels [6, 11]. The 3-axis system has an accuracy in the submillimeter range. The requirements for the capacitance measurement system were a small uncertainty (around ±15 fF) and a wide measurement range (a few fF to several pF) combined with a moderate temporal resolution (≤ 5 ms processing time per sensor).

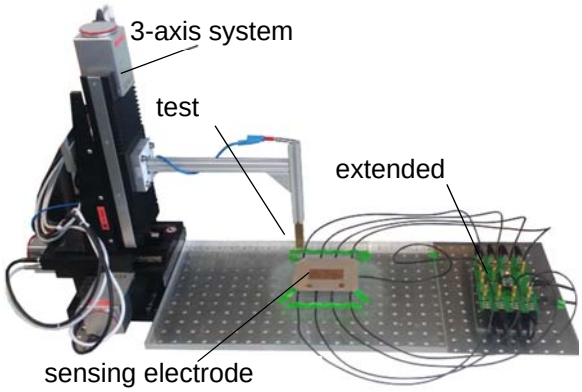

Fig. 7. Measurement system.

Fig. 8 illustrates the single and multi electrode structures (a) and (b) used as well as the grounded brass cuboid which represents a human finger. The sensing electrodes are made of a double sided PCB (printed circuit board) with an additional nanosilver imprinted PET foil at the top [12]. The sensor array (b) is based on a multilayer structure in order to circumvent interference artifacts and guarantee high symmetry.

To achieve a precise 3D localization of the test object several capacitance sensors must be combined to increase the spatial resolution (e. g., eight sensing electrodes in Fig. 8 (b)). In the set-up each electrode is connected to a separate measuring channel. The output signal of an astable multivibrator excites the sensing electrode and C_{3D} is proportional to the period of this signal. The combination of multiple sensing electrodes would decrease the accuracy for a simultaneous measurement of all channels, because the electrodes influence each other. Therefore, the sensing electrodes

[2] This is the trivial case $C_{\mathrm{sr}} = 0$.

[3] A contour line of a function of two variables is a curve along which the function has a constant value. It is a cross-section of the three-dimensional graph of the function $f(x,y)$ parallel to the xy-plane.

are evaluated sequentially. While the capacitance C_{3D} of each sensing electrode is measured all other sensing electrodes are served to the same electrical potential as the active one to eliminate the influence of parasitic capacitances between the active and inactive sensing electrodes.

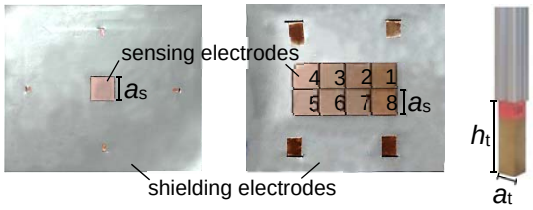

Fig. 8. Single electrode structure (a); multi electrode structure (b), and brass cuboid (c).

The left part of Fig. 9 shows a comparison of the measurement and the 3D capacitance model (26) for C_{3D} in the *xz*-plane. The right part illustrates the absolute deviation between measurement and model. The essential physical phenomena which are responsible for C_{3D} (cf. Fig. 1) are accurately described with (26) in the *xz*-plane. The absolute deviation in the short range is less than 50 fF and for larger distances much smaller (in the range of the noise). Although, in the short range the absolute deviation is highest the relative deviation is low because of the large capacitance values through the $1/z$ distance characteristics. Conversely, for larger distances the relative deviation increases.

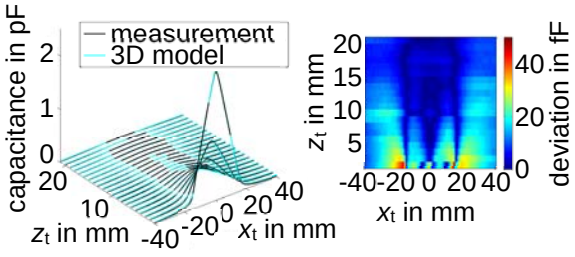

Fig. 9. Comparison of measurement and model for C_{3D} in the *xz*-plane.

Fig. 10 shows a comparison between the measurement and the 3D capacitance model (26) for C_{3D} at $z_t = 5$ mm in the *xy*-plane. The idealizations concerning the contour lines in Fig 6 cause additional deviations in comparison to the result depicted in Fig. 9. Nevertheless, Fig 10 shows that the 3D capacitance model is a good approximation for the measurement.

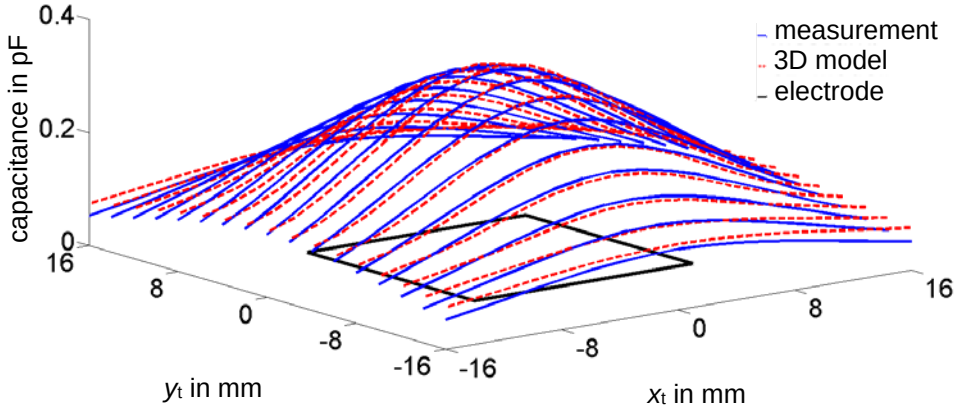

Fig. 10. Comparison of measurement and model for C_{3D} at $z_t = 5$ mm in the *xy*-plane.

4. Results

With the measured capacitance values and (26) the center position of the cuboid's base can be estimated via the formulation of an optimization problem for the measuring position as shown in preliminary studies [5]. At every sample interval the problem is viewed as quasi-stationary, and the minimization problem follows as

$$\min_{x_t,y_t,z_t} \sum_i \left(C_{m,i} - C_{3D,i}(x_t, y_t, z_t)\right)^2 \qquad (27)$$

with the measured capacitance values $C_{m,i}$ and the modeled capacitance values $C_{3D,i}$ in (26) for each measuring channel $i \in \{1...8\}$. Only the four largest capacitance values of the eight channels are used in (27) to guarantee an overdetermined well-posed problem. If further capacitance values are larger than 80 % of the least value of the initial four those are also considered to further improve the estimation.

The left part of Fig. 11 illustrates the deviation between the *x*-coordinates of the estimation and the true value of the cuboid's base while the right part of Fig. 11 shows the deviation between the *y*-coordinates. The increasing deflection in the far field

of the electrodes in Fig. 11 is caused by simplifications in the 3D capacitance model (26). Furthermore, there are also limitations of accuracy concerning the extended OpenCapSense hardware [6, 11]. The processing of the measured data by the new approach [4] results in very slight deviations from the true values (< 5 mm) close to the sensor electrodes.

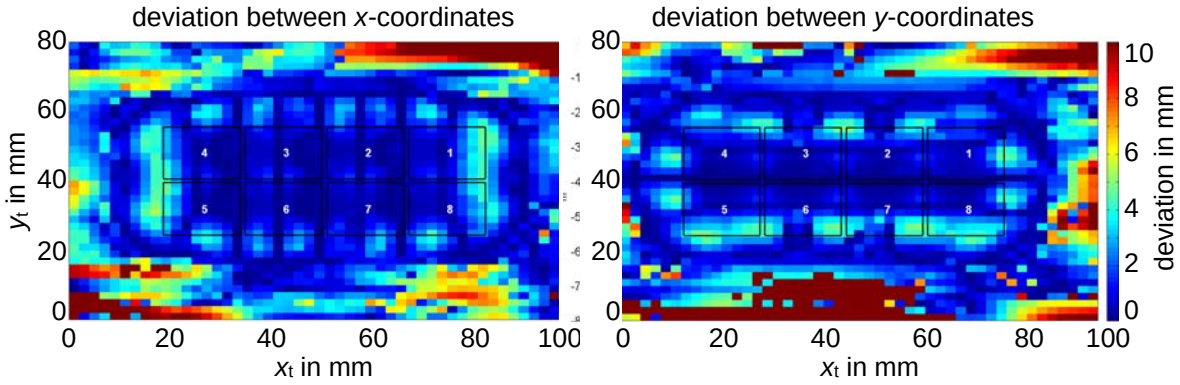

Fig. 11. Deviation of the estimated position of the coboid's base at z_t = 1 mm for x_t and y_t.

5. Conclusion

The approach used in this article can be a good basis for touchless gesture estimation of a human finger. As shown in Fig. 11 the absolute position error attainable for estimation employing the functional (27) is < 5 mm which is sufficient for a wide variety of pointing tasks. The moderate spatial resolution is sufficient still if the resolution in time is good enough to be able to follow smooth motions denoting typical swipe gestures or hand-wave gestures. Here, wipe gestures (e. g., up and down, left and right, circular forms, etc.) as known from smartphone interaction are of interest to be recognized as a user's intention. If necessary for further studies adopting parameters might be able to help to decrease absolute position errors. However, the main focus concerning capacitive proximity sensing for touchless interaction of a human finger is the application in a human machine interface.

Also an interesting point to be addressed in a future work is to investigate the validity of the assumption of a grounded metallic object as finger model and the conditions so that these this simplifications hold.

Currently the optimization problem in (27) is solved offline. Here, methods must be developed to ensure online finger gesture recognition in future research.

Acknowledgements

The authors gratefully acknowledge the partial financial support for the work presented in this paper by the Austrian Research Promotion Agency (FFG) under contract grant 846057 and WimTec Sanitärprodukte GmbH. Furthermore, we thank Simon Hehenberger for recording the measurement data.

References

[1]. A. Braun, *et al*., Capacitive sensor-based hand gesture recognition in ambient intelligence scenarios, in *Proceedings of the 6th International Conference on 'Pervasive Technologies Related to Assistive Environments'*, Rhodes, Greece, 29-31 May 2013, Article No. 5.

[2]. T. Große-Puppendahl, *et al*., Classification of User Postures with Capacitive Proximity Sensors in AAL-Environments, in *Proceedings of the International Joint Conference on Ambient Intelligence (AmI)*, *Springer,* Vol. 7040, 2011, pp. 314-323.

[3]. T. Große-Puppendahl, *et al*., Honeyfish - A High Resolution Gesture Recognition System based on Capacitive Proximity Sensing, in *Proceedings of the Embedded World Conference*, Weka Fachmedien, 2012, pp. 1-10.

[4]. L. Haslinger, B. G. Zagar, Voruntersuchungen zur berührungslosen Gestenerkennung mittels kapazitiver Sensorik, in *Proceedings of the 18th GMA/ITG Conference on 'Sensors and Measurement Systems'*, Nürnberg, Germany, 10-11 May 2016, pp. 210-217.

[5]. L. Haslinger, B. G. Zagar, 3D Position Estimation with Capacitive Sensors for Touchless Interaction, in *Proceedings of the 2nd International Conference on 'Sensors and Electronic Instrumentation Advances (SEIA' 2017)*, Barcelona, Castelldefels, Spain, 22-23 September 2016, pp. 123-127.

[6]. L. Haslinger, *et al*., Capacitance Measurement System for Touchless Interaction, in *Proceedings Eurosensor 2016*, Budapest, Hungary, 4-7 September 2016, pp. 1071-1074.

[7]. G. Durcansky, EMV-gerechtes Gerätedesign, Franzis Verlag GmbH, 1999. ISBN-10: 3772353886.

[8]. G. Willem de Jong, Smart Capacitive Sensors, Dissertation, *Delft University of Technology,* 1994.

[9]. P. Henrici, Applied and Computational Complex Analysis, *John Wiley & Son,* 1974.

[10]. N. Eidenberger, Konforme Abbildungen zur Lösung ebener inverser Probleme in der Messtechnik, Dissertation, *Johannes Kepler University Linz*, 2014.

[11]. T. Grosse-Puppendahl, *et al*., OpenCapSense: A Rapid Prototyping Toolkit for Pervasive Interaction using Capacitive Sensing, in *Proceedings of the IEEE International Conference on Pervasive Computing and Communications*, San Diego, 2013, pp. 151-158.

[12]. C. Beisteiner, B. G. Zagar, Electrical and mechanical characterization of inkjet-printed functional structures, tm - Technisches Messen, Vol. 83, Issue 11, 2016.